Investigation of 2D Boridene from First Principles and Experiments

Citation for the original published paper (version of record):

Helmer, P., Halim, J., Zhou, J. et al (2022). Investigation of 2D Boridene from First Principles and
Experiments. Advanced Functional Materials. http://dx.doi.org/10.1002/adfm.202109060

N.B. When citing this work, cite the original published paper.

(article starts on next page)

Investigation of 2D Boridene from First Principles and Experiments

Pernilla Helmer, Joseph Halim, Jie Zhou, Roopathy Mohan, Björn Wickman, Jonas Björk, and Johanna Rosen*

Recently, a 2D metal boride – boridene – has been experimentally realized in the form of single-layer molybdenum boride sheets with ordered metal vacancies, through selective etching of the nanolaminated 3D parent borides $(Mo_{2/3}Y_{1/3})_2AlB_2$ and $(Mo_{2/3}Sc_{1/3})_2AlB_2$. The chemical formula of the boridene was suggested to be $Mo_{4/3}B_{2-x}T_z$, where T_z denotes surface terminations. Here, the termination composition and material properties of $Mo_{4/3}B_{2-x}T_z$ from both theoretical and experimental perspectives are investigated. Termination sites are considered theoretically for termination species T = O, OH, and F, and the energetically favored termination configuration is identified at $z = 2$ for both single species terminations and binary termination mixes of different stoichiometries in ordered and disordered configurations. $Mo_{4/3}B_{2-x}T_z$ is shown to be dynamically stable for multiple termination stoichiometries, displaying semiconducting, semimetallic, or metallic behavior depending on how different terminations are combined. The approximate chemical formula of a freestanding film of boridene is attained as $Mo_{1.33}B_{1.9}O_{0.3}(OH)_{1.5}F_{0.7}$ from X-ray photoelectron spectroscopy (XPS) analysis which, within error margins, is consistent with the theoretical results. Finally, metallic and additive-free $Mo_{4/3}B_{2-x}T_z$ shows high catalytic performance for the hydrogen evolution reaction, with an onset potential of 0.15 V versus the reversible hydrogen electrode.

1. Introduction

2D materials have in the last couple of decades attracted a lot of interest from the research community for a broad variety of applications. The field started with the discovery of graphene in 2004,[1] followed by, i.e., hexagonal boron nitride (h-BN),[2] dichalcogenides (TMDs),[3] and MXenes.[4] Conventionally, 2D materials have been mechanically exfoliated from nanolaminated parent bulk structures in which the 2D layers are held together by weak van der Waals forces. With the discovery of MXenes, which in contrast are exfoliated by selective etching of certain atomic layers from parent 3D structures belonging to the family of MAX phases, the number of experimentally realized 2D materials has increased drastically. MXenes consist of n monoatomic layers of carbon or nitrogen (X) interleaved with $n + 1$ layers of different transition metals (M), with the surface M-layers decorated with terminations T. The chemical complexity of the MXenes gives them a great diversity in properties and possible applications.[5]

Triggered by the rapid expansion of the MXene family and the wide range of properties found in these complex materials, efforts have been made to find also other families of nanolaminated materials that could be selectively etched into 2D counterparts. One such material family is the MAB phases, where typically an A-element separates layers of M and boron (B) layers. Theoretical studies have suggested possible interesting 2D MB structures,[6,7] but it was only recently a 2D boride was experimentally realized, selectively etched from the parent i-MAB-phases $(Mo_{2/3}Sc_{1/3})_2AlB_2$ and $(Mo_{2/3}Y_{1/3})_2AlB_2$.[8] Here i stands for in plane order of the transition metals – Mo and Sc/Y – within the M layer.

Extending the realm of attainable 2D materials by a boride paves the way for exciting new research and possibilities for property tailoring by element and termination selections. In this work, we conduct further investigations on the novel 2D boride – called boridene with reference to graphene, or MBene with reference to MXene – considering basic material properties from both theoretical and experimental aspects. A detailed and comprehensive structural characterization of the boridene can be found in ref. [8]. From experience with MXenes, we know that the terminations greatly affect the material properties, which in principle could be tuned for different applications. We therefore theoretically investigate possible termination sites and perform a screening of electronic properties depending on terminating species. We find that termination with only a single terminating

P. Helmer, J. Halim, J. Zhou, J. Björk, J. Rosen
Materials Design Division
Department of Physics
Chemistry and Biology
IFM
Linköping University
Linköping 581 83, Sweden
E-mail: johanna.rosen@liu.se
R. Mohan, B. Wickman
Chemical Physics
Department of Physics
Chalmers University of Technology
Gothenburg SE-412 96, Sweden

**ADVANCED
SCIENCE NEWS**

www.advancedsciencenews.com

**ADVANCED
FUNCTIONAL
MATERIALS**

www.afm-journal.de

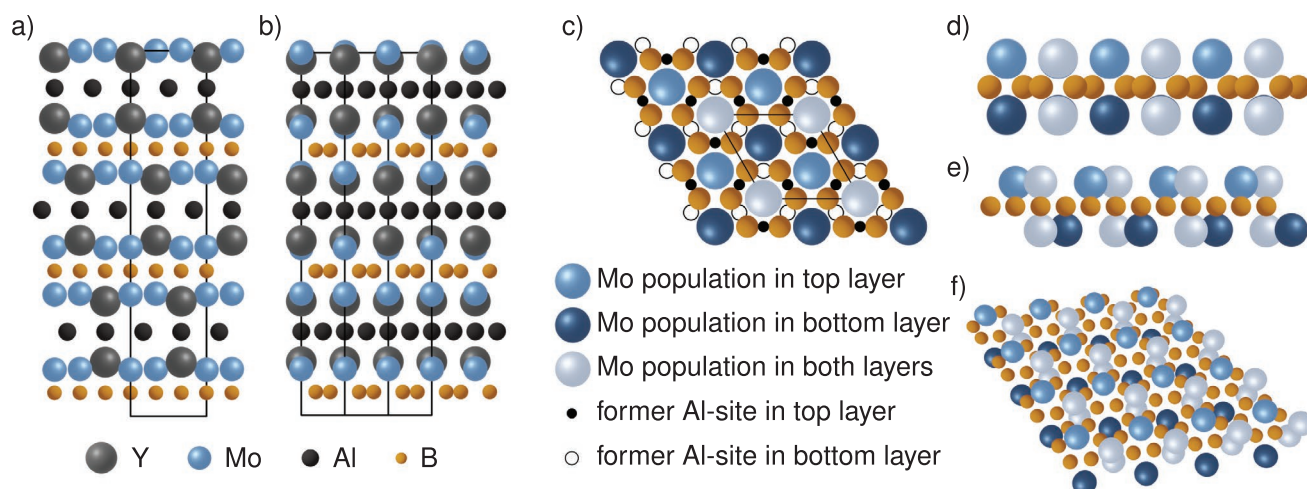**Figure 1.** Structure of the hexagonal *i*-MAB parent phase and the derived boridene without terminations. a,b) *i*-MAB structure from the [$\bar{1}$00] and [$\bar{1}$20] directions. Blue and gray, yellow and black atoms indicate Mo, Y, B, and Al respectively. c–f) Boridene without terminations from top and side views: c) [001], d) [$\bar{1}$20], e) [$\bar{1}$00]. Dark and medium blue indicate Mo atoms in bottom and top layer respectively, while light blue indicates Mo population in both layers. The black dots and circles in c) correspond to the former positions of the Al-atoms above and below the Mo–B–Mo layer, respectively. These positions correspond the bridge between populated Mo sites in each layer.

species gives rise to semiconducting properties with a small to vanishing bandgap, while for mixed species termination a metallic or possibly semiconducting behavior can be observed. While the theoretical results are relevant for a boridene derived from both $(Mo_{2/3}Sc_{1/3})_2AlB_2$ and $(Mo_{2/3}Y_{1/3})_2AlB_2$, the experimental analysis is performed on 2D material from selectively etched $(Mo_{2/3}Y_{1/3})_2AlB_2$. A detailed composition analysis using X-ray photoelectron spectroscopy (XPS), complementary to that of the original paper,[8] gives a chemical formula of $Mo_{1.33}B_{1.9 \pm 0.2}O_{0.3 \pm 0.1}(OH)_{1.5 \pm 0.2}F_{0.7 \pm 0.1}0.2 \pm 0.05H_2O_{ads.}$, with a total termination concentration of $z = 2.5 \pm 0.5$. Optical property measurements are also presented, indicating a metallic material.

Further, we demonstrate $Mo_{4/3}B_{2-x}T_z$ as a promising material for hydrogen evolution in acidic conditions with an onset potential of 0.15 V versus the reversible hydrogen electrode (RHE) and with no degradation after 67 h of hydrogen evolution at 10 mA cm^{-2}, which is superior to most non-Pt containing materials as well as emerging 2D materials, including MXenes.

2. Structure Description

The boride 2D structure synthesized in ref. [8] is derived from the recently discovered hexagonal 3D *i*-MAB phases $(Mo_{2/3}Y_{1/3})_2AlB_2$ and $(Mo_{2/3}Sc_{1/3})_2AlB_2,$[9] by selective etching of the Al and Y/Sc species. The hexagonal *i*-MAB structure can be seen from the [-1-10] and [-1-20]-directions in **Figure 1**a,b; it is built up by layers consisting of a boron (yellow) honeycomb lattice decorated with two different transition metals (M) – Y (gray) and Mo (blue) in this particular case – interleaved with Al (black) atoms arranged in a Kagomé lattice. The 2D structure attained by selective etching, hereinafter referred to as boridene, is shown schematically without terminations in Figure 1c–f. The removal of Al and Y in the etching process leaves a hexagonal boridene of the ideal formula $Mo_{4/3}B_2$, which

consists of 3 atomic layers stacked as Mo–B–Mo. The sites populated by Y in the parent *i*-MAB structure form vacancies in the derived boridene. These vacancies are misaligned between the two Mo layers of the boridene, since the Y-atoms in the M–B–M layers of the *i*-MAB structure are misaligned along the z-axis, occupying different positions in the top and bottom Mo layer. In Figure 1c–f, Mo population and vacancies are implied by a different color of the Mo atoms; dark and medium blue atoms populate Mo sites in the bottom respectively top layer, with vacancies in the opposite layer. The light blue atoms indicate sites occupied in both layers and thus have no associated vacancy. The vacancies are clearly seen in Figure 1f where Mo atoms in respective layer form two honeycomb lattices which are shifted with respect to each other. The black dots and circles in Figure 1c indicate the former positions of the removed Al atoms in the layer above and below the boridene, respectively.

2.1. Termination Coverage

When chemically exfoliating a 2D structure from a 3D parent phase, new atomic species, or functional groups, referred to as terminations, attach to the surface of the 2D structure. For the MXene family, where terminations have been extensively studied, a termination concentration of one termination (T) per surface metallic site is expected, giving the formula $M_{n+1}X_nT_2$.[5] For the boridene studied here, this would translate to an ideal formula of $Mo_{4/3}B_2T_2$. In the definition of "metallic site," we thus include the vacancies from the Y atoms, as in the case for MXenes with metal vacancies, also referred to as *i*-MXenes.[10,11] This extrapolation is compatible with the hexagonal symmetry of the boridene and is supported by initial computational studies presented in Section S1.2 and Figures S1 and S2 of the Supporting Information.

The experimentally attained chemical formula reported for the boridene is $Mo_{4/3}B_{2-x}T_z$, indicating possible boron vacancies and an unknown termination (T) concentration.
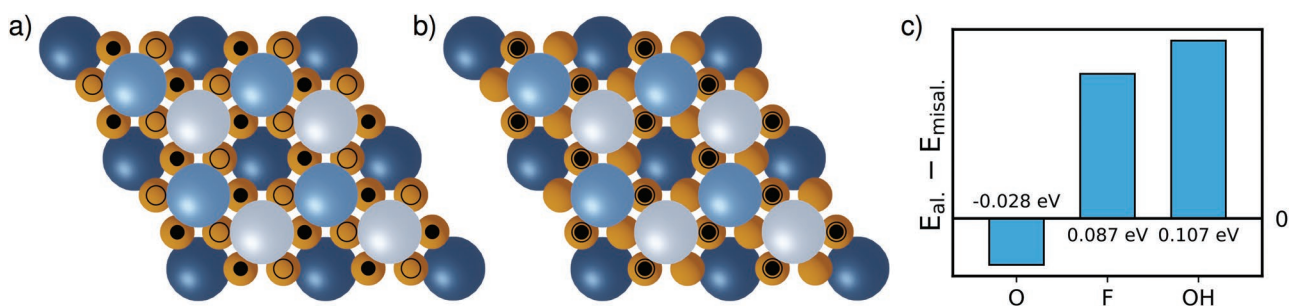
Figure 2. Schematic structure of a) misaligned and b) aligned termination configurations. Black dots indicate terminations at the top layer and black rings indicate terminations at the bottom layer. Yellow atoms represent boron, while light blue, medium blue, and dark blue represent Mo in both, top and bottom layers, respectively. c) Energy difference between misaligned and aligned structures for the three single species structures. The line indicates the misaligned configurations, with energy given in eV per formula unit (f.u.). The blue bars show the difference to the aligned configurations. The misaligned configuration is energetically favorable for F and OH terminations, while the aligned configuration is favored for O terminations.

From EELS analysis performed in the seminal study, the proposed approximate formula for a single sheet of boridene is $Mo_{1.33}B_{1.55}O_{2.66}$ with some traces of F, while initial XPS analysis on a freestanding film suggests that the three termination types O, F, and OH are present. Observed point defects and a flake size of up to 50 nm give that the ideal formula of $Mo_{4/3}B_2T_2$ is within the experimental error margin of the original work.[8] For the sake of simplicity, we initially disregard the implication of boron vacancies, thus considering structures of the ideal formula $Mo_{4/3}B_2T_2$, with the primitive cell constituted of three such formula units.

2.2. Termination Sites

Initial studies were performed to map the topological energy landscape of O- and F-adsorbates to the boridene surface, a detailed presentation and discussion can be found in Section S1 (Supporting Information). The primarily considered sites were on top and below of the B atoms (B sites), on top and below of the two different Mo atoms and the Y vacancies (Mo sites), and on the bridge between populated Mo sites in respective layer (bridge sites). The bridge sites are the same as the positions of the former Al-atoms, indicated in Figure 1c by black dots and circles. Other sites proved unstable upon structural relaxation or energetically disadvantageous. The possible ways to attain a termination concentration of $z = 2$ with these sites are either through full population of bridge sites, full population of all three Mo sites, or half population of B sites. The latter can be arranged in two distinct configurations, shown in **Figure 2**a,b, respectively. The configuration in a) has terminations centered on top of every second B site (black dots) and below every other B site (black circles), so that every B site can be associated with one termination. This is referred to as the "misaligned" configuration. The configuration in b) has instead terminations centered on top and below of every second B site, so that every second B site is associated with two terminations and every other with none. This is referred to as the "aligned" configuration. Hence, in total four different configurations with $z = 2$ were considered in these initial studies, where the B-site configurations proved to be energetically favored regardless of terminations species.

3. Optimization and Dynamical Stability of Ideal Structures with Single Species Terminations: $Mo_{4/3}B_2T_2$, T = F, O, or OH

Once the B site at half population ($z = 2$) was found to be the preferred termination site, both the aligned and misaligned configurations were investigated in some more detail for the three experimentally detected termination species: O, F, and OH. In the following, $z = 2$ will be referred to as "full termination," and full termination of the boridene with a single termination species, i.e., $Mo_{4/3}B_2O_2$, $Mo_{4/3}B_2F_2$, or $Mo_{4/3}B_2(OH)_2$, are referred to as single species termination.

The dynamical stability of the single species terminated boridene was investigated for both the misaligned and aligned configurations, schematically shown in Figure 2a,b. After corrections to ensure rotational and translational invariance of the force constants, by enforcing the Born–Huang sum rules and Huang condition, all single species termination structures were found to be dynamically stable. The dynamical stability of the unterminated boridene $Mo_{4/3}B_2$ was also studied, showing that the structure is unstable without terminations. The phonon spectra are shown in Figures S3 and S4 (Supporting Information). Although both single species termination configurations are stable for all three termination species, the energy differs between the two configurations, shown in Figure 2c. For $Mo_{4/3}B_2F_2$, and $Mo_{4/3}B_2(OH)_2$ the misaligned configuration is energetically favored to the aligned, with 87 and 107 meV(f.u.)$^{-1}$ respectively. For $Mo_{4/3}B_2O_2$ the aligned configuration is favored with 28 eV(f.u.)$^{-1}$. The energetically favored configuration for each termination species is presented in **Figure 3**. In $Mo_{4/3}B_2O_2$, shown in Figure 3a, the terminations are not positioned at the ideal sites indicated in Figure 2b, but rather positioned to the side of the B sites toward the bridge sites in the respective layer. The bridge sites are not shown but indicated in Figure 1c. For $Mo_{4/3}B_2F_2$, shown in Figure 3b, the F terminations are on the other hand close to their ideal positions. Finally, for $Mo_{4/3}B_2(OH)_2$, shown in Figure 3c, each hydroxyl group is positioned with the O atom close to the ideal site, and the H almost at the bridge site. The hydroxyl groups are thus oriented with their symmetry axis tilted with respect to the normal of to the boridene surface.
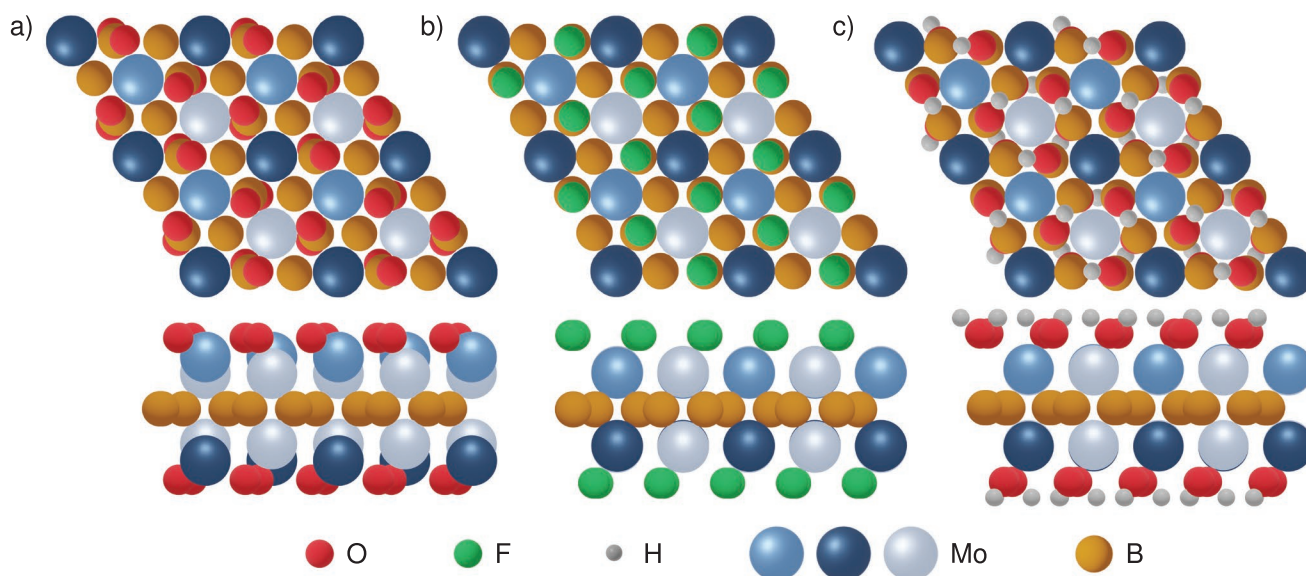
**ADVANCED
SCIENCE NEWS**
www.advancedsciencenews.com

**ADVANCED
FUNCTIONAL
MATERIALS**
www.afm-journal.de

Figure 3. Fully relaxed energetically favored single species termination configurations. a) Aligned $Mo_{4/3}B_2O_2$. The O-atoms sit to the side of the B site, toward the bridge site. b) Misaligned $Mo_{4/3}B_2F_2$, the F atoms are very close to the ideal sites schematically shown in Figure 2a. The F atoms in the bottom layer are not visible. c) Misaligned $Mo_{4/3}B_2(OH)_2$, in which the O atoms are close to the ideal misaligned configuration in Figure 2a and with the OH-bond pointing such that the H-atoms are positioned close to the bridge site.

3.1. Optimization and Dynamical Stability of Single Species Terminations with Boron Vacancies: $Mo_{4/3}B_{2-x}T_2$, $x = 1/3, 2/3$

The original EELS investigations of a single sheet suggest the possibility of boron vacancies and propose an approximate chemical formula of $Mo_{1.33}B_{1.55}O_{2.66}$ for the boridene, i.e., a boron deficiency of $x = 0.45$ atoms f.u.$^{-1}$ compared to the ideal formula of $Mo_{4/3}B_2T_2$, and with an excess of oxygen terminations. Still, F terminations could not be excluded. It should be noted that the boridene flakes were comparatively small (up to 50 nm) compared to those observed in the more mature research field of MXenes. Furthermore, point defects other than the ordered vacancies could be observed, arising from the synthesis procedure or from the conditions under which the TEM analysis was performed. Thus, we conducted a brief investigation of vacancy structures, considering both O and F terminations. OH was disregarded at a first approximation, motivated by the valence electron configuration being similar to F. Boron vacancies were modeled on the single unit cell, with full termination and $x = 1/3$ and $2/3$ in $Mo_{4/3}B_{2-x}T_2$.

For both terminations (T = O, F) and boron vacancy concentrations ($x = 1/3, 2/3$), the structures were found to approximately preserve the hexagonal pattern of the Mo atoms, with schematics of the structures presented in Figure S5 (Supporting Information). In finding the energetically most favorable structures for each stoichiometry, both the aligned and misaligned termination configurations were considered. For $Mo_{4/3}B_{2-x}T_2$ with T = F, the resulting structures shown in Figure S5b,c (Supporting Information) are close to $Mo_{4/3}B_2F_2$ besides the missing boron atoms, while for T = O the resulting structures are quite distorted from the initial configuration, although still approximately retaining a hexagonal pattern in the Mo atoms, as can be seen in Figure S5e,f (Supporting Information).

Although T = F seems more plausible from the visual study of the structures in Figure S5 (Supporting Information), only those with T = O were found dynamically stable, while for T = F the lowermost branch showed considerable areas of imaginary frequencies for both vacancy concentrations. The corresponding phonon spectra are found in Figure S6 (Supporting Information). The result that only O terminations yield stable structure agrees with the EELS data from ref. [8], which showed in principle only O terminations. However, for both vacancy concentrations with T = O, structures were found that had a lower total energy than those presented in Figure S6e,f, (Supporting Information), but all were gravely distorted from the hexagonal pattern and were therefore not considered further. Thus, the attained structures for T = O are at best thermodynamically metastable. Considering the distortion of the attained O terminated boron vacancy structures and their thermodynamical instability, together with the results from the XPS analysis presented in the following section, we chose to focus the investigations of this work on the ideal formula $Mo_{4/3}B_2T_2$ and not consider vacancies further. A more detailed discussion around and motivation for this can be found at the end of the next section.

4. XPS Analysis

A detailed XPS analysis was performed, complementary to that of the original paper, to determine the chemical formula for filtered films of the boridene. To attain a reliable quantitative analysis, especially for the boron content, XPS measurements were performed on a reference MoB sample, in which the composition ratio was obtained as 1 Mo: 0.97 ± 0.04 B, which is close to the expected 1 Mo:1 B.
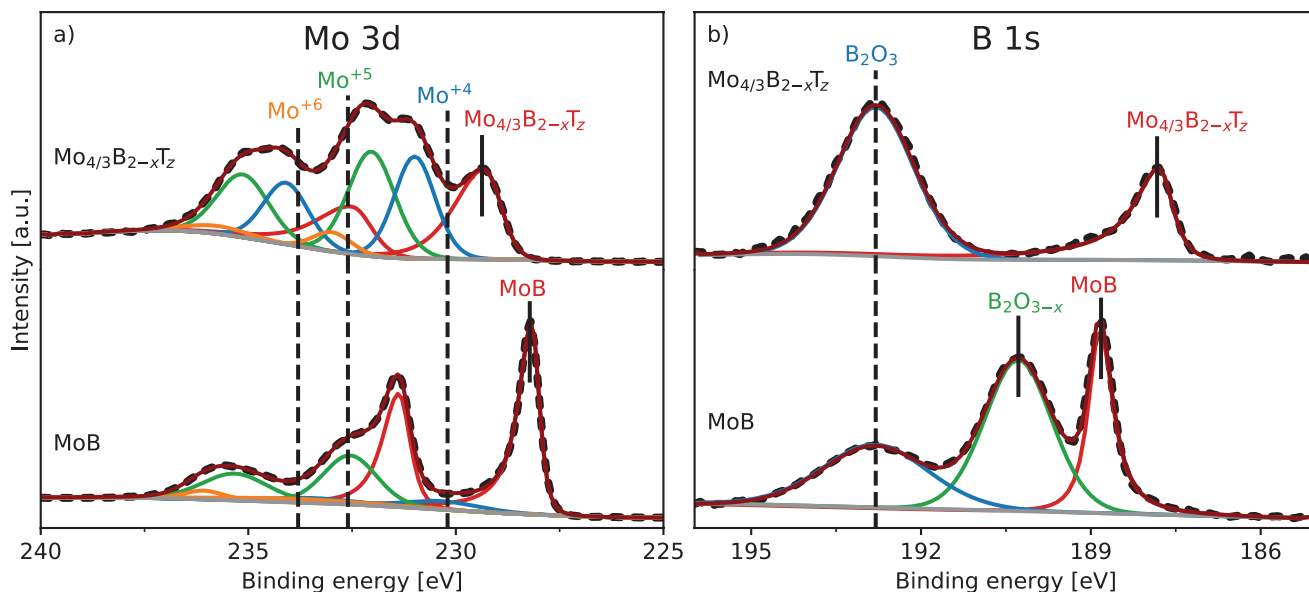
Figure 4. High-resolution XPS spectra of a) Mo 3d and b) B 1s regions for $Mo_{4/3}B_{2-x}T_z$ filtered film (top) and MoB cold pressed reference sample (bottom) along with their fittings representing various species.

Figure 4 shows high-resolution XPS data of the Mo 3d region in a) and the B 1s region in b) for $Mo_{4/3}B_{2-x}T_z$ and MoB. The boridene data are shown in the top spectra of each panel, and MoB data in the bottom spectra. Table S1 (Supporting Information) shows the obtained global atomic percentages from the analysis. In Figure 4a we can see that in the Mo 3d region, the binding energy (BE) for the peak corresponding to the Mo species in the boridene, labeled $Mo_{4/3}B_{2-x}T_z$ and shown in red in the top spectrum, is shifted toward higher energies by 1.1 eV compared to that belonging to MoB in the bottom spectrum. The BE of the Mo species in the boridene is shifted by 0.6 and 1.3 eV with respect to that in $(Mo_{2/3}Y_{1/3})_2AlB_2$ and metallic Mo, which are shown in ref. [8] and Figure S7 (Supporting Information), respectively. This shift indicates a decrease in the metallic bonding nature of the Mo species in the boridene compared to that in the precursor $(Mo_{2/3}Y_{1/3})_2AlB_2$, which is due to the removal of Al and most of the Y from the precursor, where the bonds between both Y and Al with Mo are metallic. The surface terminations attaching to the 2D flake during etching (O, F, and OH, shown in Figure S8 and Table S2, Supporting Information) form bonds of a more covalent nature to the Mo species.

The BE for the peak in the B 1s region corresponding to the B species in the boridene, shown in red in the top spectrum of Figure 4b, is instead shifted towards lower energies by 1.0 eV compared to that in MoB, shown in Figure 4b bottom spectrum, and by 0.4 eV compared to $(Mo_{2/3}Y_{1/3})_2AlB_2$.[8] This shift might be due to the vacancies in the Mo layers, caused by the removal of Y during etching, which may shift the B bonding nature towards elemental B (BE = 187.2 ± 0.2 eV, not shown).[8,12] The XPS spectra along with their fitting results for the rest of the XPS regions, Y 3d, Al 2p, O 1s, and F 1s for the boridene are shown in Figure S8 and Table S2 (Supporting Information). The chemical formula for the boridene was calculated from the XPS

analysis, with detailed information to be found in Section S3 of the Supporting Information, to be:

$$Mo_{4/3}B_{1.9\pm0.2}O_{0.3\pm0.1}(OH)_{1.5\pm0.2}F_{0.7\pm0.1}0.2\pm0.05H_2O_{ads}.$$
$$\text{total } T_z = 2.5 \pm 0.5$$
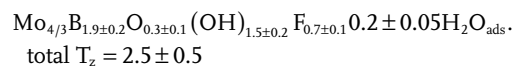
The analysis is based on several assumptions, as detailed in the Supporting Information. Trace amounts of Y can also be detected, though this is below 0.1 moles per mole of $Mo_{4/3}B_{2-x}T_z$. These results are in contrast with the EELS analysis of ref. [8], which suggested boron vacancies and primarily O terminations. However, the two different analyses are performed in different environments and represent global and local analysis, respectively. During an EELS measurement, the sample consists of a single flake, is kept in a vacuum, bombarded with electrons and kept at a temperature well above room temperature. During an XPS measurement, the sample instead consists of a filtered film of multiple 2D flakes and is kept at room temperature. We chose to focus the continued theoretical investigations on the average composition space suggested by the XPS measurements, rather than that of the EELS analysis in ref. [8].

5. Mixed Species Terminations:Binary Termination Mixing

With more accurate data attained from the refined XPS analysis, it is clear that the boridene can be expected to have terminations of different species, and thus the single species termination is more of qualitative than quantitative interest for the present work, while still indicating future tuning potential of the material's composition and related properties. In the following, have therefore addressed the possibility
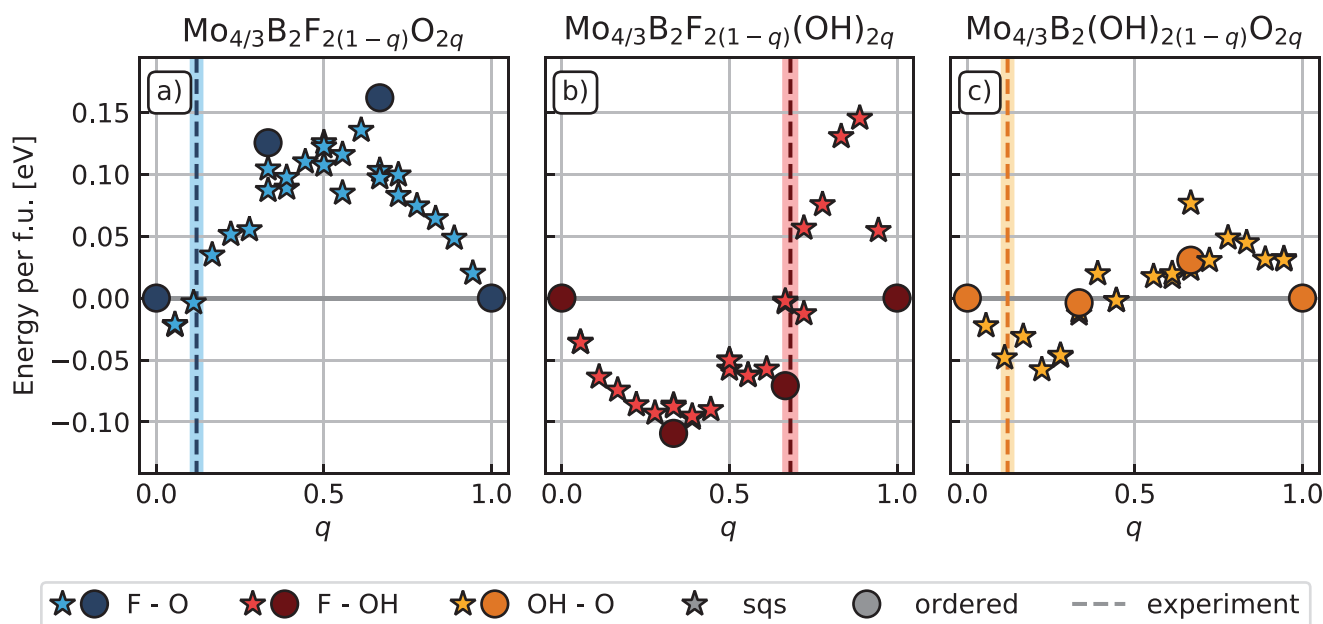
**ADVANCED
SCIENCE NEWS**

www.advancedsciencenews.com

**ADVANCED
FUNCTIONAL
MATERIALS**

www.afm-journal.de

Figure 5. Energy deviation in eV f.u.$^{-1}$ for mixed species termination configurations from linear combination of single species termination configurations with same total stoichiometry at room temperature ($T = 300$ K). All three binary termination combinations have been considered: a) $Mo_{4/3}B_2F_{2(1-q)}O_{2q}$, b) $Mo_{4/3}B_2F_{2(1-q)}(OH)_{2q}$ and c) $Mo_{4/3}B_2(OH)_{2(1-q)}O_{2q}$. The dashed lines imply experimentally observed fractions from the refined XPS-analysis.

for mixed species termination by considering termination adsorption energy for ordered and disordered termination configurations. To limit the parameter space and make the calculations more feasible, only binary termination mixes were considered. For the ordered mixed species termination, the terminations were placed in both the aligned and misaligned configurations on the single unit cell, with data presented for the energetically most favorable configuration. All but $Mo_{4/3}B_2(OH)_{2/3}O_{4/3}$ were found to prefer the misaligned configuration, the favored configuration for each stoichiometry is shown in Figure S9 (Supporting Information). When studying disorder, only the misaligned configuration was considered, since this was the preferred configuration for five out of the six different mixed species termination stoichiometries considered.

5.1. Comparison of Ordered and Disordered Structures

Figure 5 shows a diagram over the Gibbs free energy of formation ΔG_q of the three different binary termination mixtures $Mo_{4/3}B_2F_{2(1-q)}O_{2q}$ (blue), $Mo_{4/3}B_2F_{2(1-q)}(OH)_{2q}$ (red), and $Mo_{4/3}B_2(OH)_{2(1-q)}O_{2q}$ (yellow). The free energy ΔG_q is defined as:

$$\Delta G_q = \Delta H_q - T\Delta S_q \qquad (1)$$

where T is temperature and ΔS_q is the configurational entropy, as given by Equation (3). The formation enthalpy ΔH_q is defined with respect to the single species terminated structures:

$$\Delta H_q = E_{mix}^{1,2}(q) - qE_1 - (1-q)E_2 \qquad (2)$$

$E_{mix}^{1,2}(q)$ is the total electronic energy of the binary species termination mix with terminations T_1 and T_2, at a fraction q of termination T_1 and $(1-q)$ for termination T_2. E_1 and E_2 are the total energies of the single species terminated boridene for respective termination species. All energies are given per formula unit, and the temperature $T = 300$ K was used for the evaluation of ΔG_q.

For $Mo_{4/3}B_2F_{2(1-q)}O_{2q}$, shown in blue in Figure 5a, mixed species termination is only favorable to single species termination at small fractions q, i.e., at high fractions of F terminations/low fractions of O terminations. Disordered configurations (stars) are favored over the ordered mixed species termination configurations at $q = 1/3$ and $q = 2/3$ (circles). The vertical dashed line indicates the experimentally observed total O fraction corresponding to $q = 0.3/2.5 = 0.12$, obtained from the XPS analysis presented above, with the shaded area indicating error margins.

For $Mo_{4/3}B_2F_{2(1-q)}(OH)_{2q}$, shown in red in Figure 5b, mixed species termination is energetically favorable to single species termination for a considerable range of fractions from $q > 0$ to approximately $q = 0.7$. For this system, as opposed to $Mo_{4/3}B_2F_{2(1-q)}O_{2q}$, order seem to be preferred over disorder. The dashed line indicates again expected composition from the refined XPS analysis at $q = 0.7/2.2 = 0.68$, with the shaded area indicating error margins. Only the relative fraction of F and OH terminations has been considered for the evaluation of this number, ignoring O terminations.

For $Mo_{4/3}B_2(OH)_{2(1-q)}O_{2q}$, shown in yellow in Figure 5c, the implications are not quite as clear. For $q > 0.5$, mixed species termination is disfavored to single species termination, while for $q < 1/3$, mixed species termination is preferred. There are no clear implications of whether order or disorder is preferred. The experimentally observed O fraction of $q = 0.12$ is again indicated.
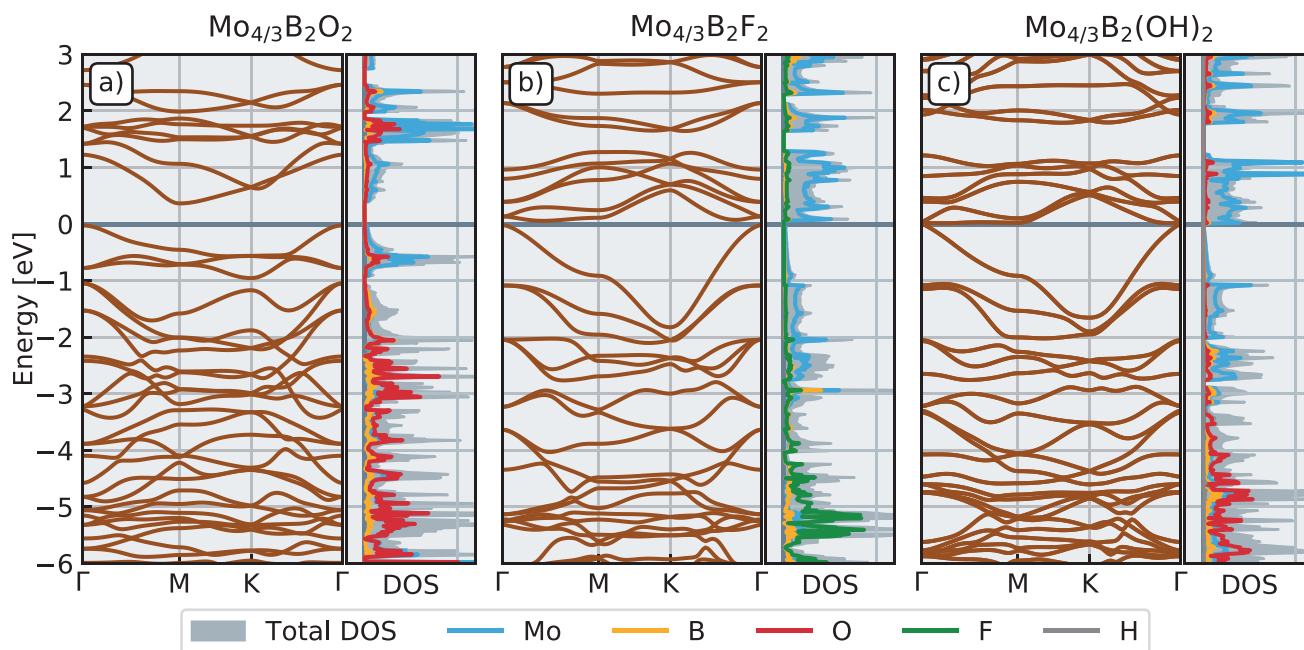
**ADVANCED
SCIENCE NEWS**

www.advancedsciencenews.com

**ADVANCED
FUNCTIONAL
MATERIALS**

www.afm-journal.de

Figure 6. Band structure and density of states (DOS) for a) $Mo_{4/3}B_2O_2$, b) $Mo_{4/3}B_2F_2$ and c) $Mo_{4/3}B_2(OH)_2$. All three structures display a bandgap at the Fermi level, of ≈ 0.3 eV, ≈ 0.08 eV, and <0.02 eV, respectively.

For $Mo_{4/3}B_2F_{2(1-q)}O_{2q}$ and $Mo_{4/3}B_2F_{2(1-q)}(OH)_{2q}$ the experimentally observed fractions match well with the disordered mixed species termination being energetically equivalent to separation into single species termination, while for $Mo_{4/3}B_2(OH)_{2(1-q)}O_{2q}$ the experimental line is close to the minima of the mixed species termination curve. This is encouraging in that the theoretical results are not in disagreement with experiments.

For ordered configurations, the energetically favored structure for each set of (T_1, T_2, q) is shown in Figure S9 (Supporting Information). All of these were found to be dynamically stable, with the phonon spectra shown in Figure S10 (Supporting Information).

6. Electronic Structure

The electronic structures of all presented ordered structures have been evaluated, band structures for single species termination configurations are shown in **Figure 6**, and for mixed species termination configurations in **Figure 7**.

In Figure 6a,b, the band structures for $Mo_{4/3}B_2O_2$ and $Mo_{4/3}B_2F_2$ display indirect bandgaps of ≈ 0.3 and ≈ 0.08 eV, respectively. For $Mo_{4/3}B_2(OH)_2$, shown in Figure 6c, it is difficult to resolve a gap between the valence and conduction bands, at the same time as the density of states diminishes at the top of the valence band, indicating a semi-metallic behavior. However, considering the well known underestimation of bandgaps in semi-local DFT such as the GGA invoked for the current computations, the actual bandgaps are likely considerably larger than what is found here.

Studying the characteristics of band structures and DOS, $Mo_{4/3}B_2F_2$ and $Mo_{4/3}B_2(OH)_2$ have clear similarities, supporting

the assumption that the equal valency of F and OH would result in similar behavior. For the highest energy valance states the DOS is governed by a single Mo band with high dispersion, and the DOS increases slowly until -1 eV, where the second and third highest valance bands appear. This, together with the negligibly sized bandgap indicate that these structures will in principle act as poor conductors. Both below and above the Fermi level the hybridization is low for these structures, and the DOS is dominated by Mo states.

The electronic structure for $Mo_{4/3}B_2O_2$ shown in Figure 6a is significantly different compared to that of $Mo_{4/3}B_2F_2$ and $Mo_{4/3}B_2(OH)_2$. O has 1 electron less than F and OH, causing the unit cell of $Mo_{4/3}B_2O_2$, which consists of 3 formula units, to have 6 electrons less than $Mo_{4/3}B_2F_2$ and $Mo_{4/3}B_2(OH)_2$, and thus the Fermi level will be 3 bands lower for $Mo_{4/3}B_2O_2$. At the Fermi level, a small bandgap has opened where there was only a minimum in the DOS for $Mo_{4/3}B_2F_2$ and a much smaller gap for $Mo_{4/3}B_2(OH)_2$. The states down to -1 eV consist of hybridization between all three atomic species, as opposed to in $Mo_{4/3}B_2F_2$ and $Mo_{4/3}B_2(OH)_2$ where Mo dominated the states down to -2 eV. Between -2 to -6 eV hybridization between states is more pronounced for all three configurations.

Looking at the band structures for the mixed species termination configurations, shown in Figure 7, we see that $Mo_{4/3}B_2F_{2(1-z)}O_{2z}$ and $Mo_{4/3}B_2(OH)_{4/3}O_{2/3}$ show metallic behavior, which was not seen for the single species terminations. Furthermore, the $Mo_{4/3}B_2F_{2(1-z)}(OH)_{2z}$ configurations have band structures very similar to that of $Mo_{4/3}B_2F_2$ and $Mo_{4/3}B_2(OH)_2$, which can be attributed to these structures having the same valency. The valance band is dominated by Mo states just as for $Mo_{4/3}B_2F_2$ and $Mo_{4/3}B_2(OH)_2$. $Mo_{4/3}B_2(OH)_{2/3}O_{4/3}$, which is the only structure with terminations in the aligned configuration, displays a bandgap at the

**ADVANCED
SCIENCE NEWS**
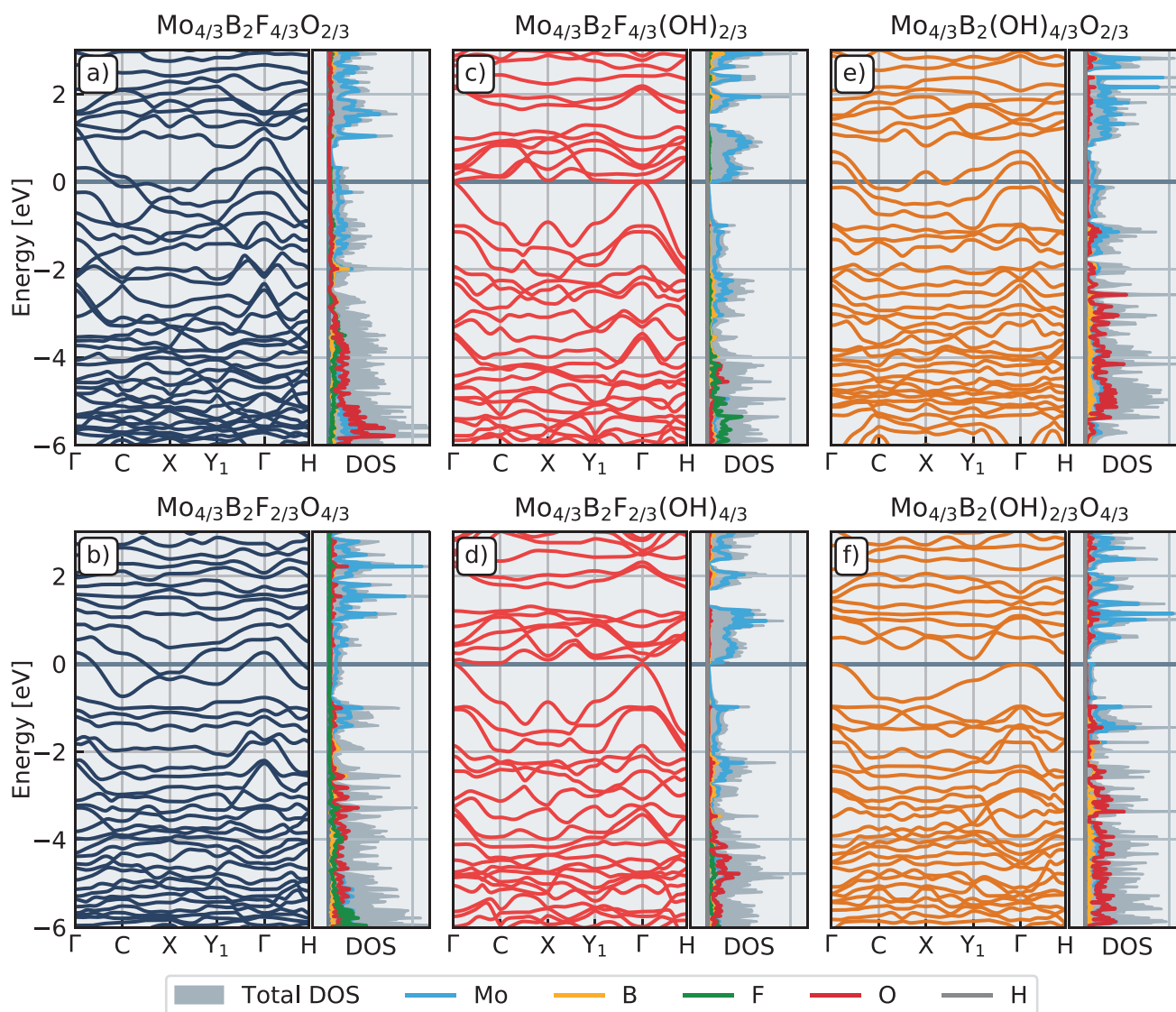
www.advancedsciencenews.com

**ADVANCED
FUNCTIONAL
MATERIALS**

www.afm-journal.de

Figure 7. Band structure and density of states (DOS) for a) $Mo_{4/3}B_2F_{4/3}O_{2/3}$, b) $Mo_{4/3}B_2F_{2/3}O_{4/3}$, c) $Mo_{4/3}B_2F_{4/3}(OH)_{2/3}$, d) $Mo_{4/3}B_2F_{2/3}(OH)_{4/3}$, e) $Mo_{4/3}B_2(OH)_{4/3}O_{2/3}$, and f) $Mo_{4/3}B_2(OH)_{2/3}O_{4/3}$. All but $Mo_{4/3}B_2(OH)_{2/3}O_{4/3}$ prefer the misaligned configuration.

Fermi level, despite having a different valency from all the single species termination structures.

Initial assessment of the optical properties for a colloidal solution of $Mo_{4/3}B_{2-x}T_z$, which after filtering produces the herein analyzed film of composition $Mo_{1.33}B_{1.9\pm0.2}O_{0.3\pm0.1}(OH)_{1.5\pm0.2}F_{0.7\pm0.1}0.2\pm0.05H_2O_{ads.}$, is shown in Figure S11 (Supporting Information). The results show no distinct transition peaks, and thus suggest a metallic behavior of the material.

7. Hydrogen Evolution Reaction

$Mo_{4/3}B_{2-x}T_z$ is very interesting for energy applications as it is composed of abundant materials and the 2D form allows very high materials utilization.[13] Here, we have investigated the potential of 2D $Mo_{4/3}B_{2-x}T_z$ as cathode catalyst material for elec-

trochemical hydrogen production via the hydrogen evolution reaction (HER) in acidic media. The activity for the HER was evaluated by cyclic voltammetry in 0.5 M H_2SO_4 using a rotating disc electrode (RDE) setup. The onset potential of HER was taken at the potential at which the current reached –1 mA cm^{-2} in the cathodic scan. As seen in **Figure 8**, the as-deposited $Mo_{4/3}B_{2-x}T_z$ showed an activity for HER, with an initial onset potential around –0.4 V versus RHE. However, after successive cycling and a 67 h constant current experiment at –10 mA cm^{-2}, shown in Figure S12 (Supporting Information), the HER activity increased significantly, shifting the onset to –0.15 V versus RHE, which is an impressive number for a non-Pt material.[14] Furthermore, Tafel analysis shown in Figure S14 (Supporting Information) revealed a low Tafel slope during HER, between 24 and 27 mV dec^{-1}. Further details of the measurement and the analysis are given in Figures S12–S16 (Supporting Information). It should be noted that no sign of degradation was observed during the 67 h
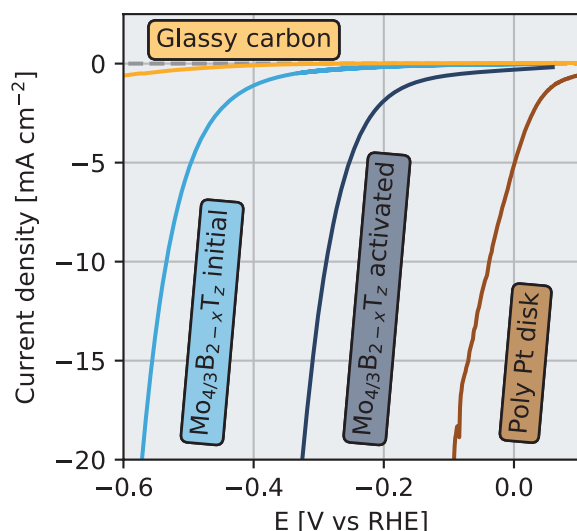
Figure 8. Hydrogen evolution reaction (HER) polarization curves of 2D $Mo_{4/3}B_{2-x}T_z$ sheets compared with polycrystalline Pt and glassy carbon (GC) disk at 50 mV s^{-1} scan rate in 0.5 M H_2SO_4.

chronopotentiometry measurement, as can be seen in Figure S12 (Supporting Information). Electrochemical impedance spectroscopy (EIS) was employed to study the electrocatalytic activity for the as deposited and activated samples, as shown in Figure S16 (Supporting Information). The lower value for the charge transfer resistance, R_{ct}, found for the sample after 67 h activation corroborates both the Tafel slope and the HER activity. It was observed that the activity for HER was increased as a consequence of subjecting the material to cathodic potentials. At the mild cathodic conditions during the 67 h measurement at -10 mA cm^{-2} the activity increase was rather slow (hours) while cycling to more cathodic potentials increased the activity much faster (minutes). Upon subjection to anodic potentials up to 0.4 V versus RHE the activity for HER was dramatically reduced. However, subsequent cathodic treatment restored the HER activity, indicating that the activity increase upon cathodic potentials and activity decrease upon anodic potentials were reversible. This observation is important since the reversibility shows that the behavior is not caused by significant structural changes, such as a phase transformation, in the material. A potential explanation for the increased activity of the boridene during exposure to reductive conditions might be proton absorption into the vacancies at cathodic potentials, as recently suggested for a 2D $W_{1.33}C$ i-MXene.[15] Altogether, the high stability and good HER performance of the boridene suggests a promising new family of nonprecious metal-based electrocatalysts for HER in low pH conditions.

8. Conclusions

We have presented a combined computational and experimental study addressing on fundamental aspects of the recently discovered 2D material boridene, $Mo_{4/3}B_{2-x}T_z$, particularly focusing on termination site, composition, and electronic structure, as well as demonstrating the proficiency of boridene for the hydrogen evolution reaction. The surface terminations of

boridene were found to prefer populating sites directly above/below the B sites, in an aligned configuration for $Mo_{4/3}B_2O_2$, while a misaligned configuration is preferred for $Mo_{4/3}B_2F_2$ and $Mo_{4/3}B_2(OH)_2$. A detailed XPS analysis provided a composition of $Mo_{4/3}B_{1.9\pm0.2}O_{0.3\pm0.1}(OH)_{1.5\pm0.2}F_{0.7\pm0.1}0.2 \pm 0.05H_2O_{ads}$, with a total number of terminations of $z = 2.5 \pm 0.5$ per formula unit. This is within the theoretically considered termination coverage of $z = 2$. The energies of both ordered and disordered mixed species termination configurations considering binary mixes were compared to structures with single species terminations, and were found to be energetically favorable to single species for some concentration ranges. The dynamical stability of all ordered structures presented was evaluated, and all were found to be dynamically stable. The results are consistent with experiments and show a large variety in possible termination compositions.

The band structures of both single and ordered mixed species structures were evaluated theoretically, showing that the boridene may exhibit metallic, semimetallic or semi insulating behavior with a direct or indirect bandgap, all depending on the specific configuration and composition of terminations. This suggests rich opportunities for tailoring the electronic properties of the boridene for different purposes. Optical property measurements indicated metallic behavior specifically for the experimentally analyzed film, and it was shown that the additive-free $Mo_{4/3}B_{2-x}T_z$ has high catalytic performance for the hydrogen evolution reaction, with an onset potential of 0.15 V with respect to the reversible hydrogen electrode.

9. Computational and Experimental Section

Computational Details: The electronic structure computations were done within the framework of periodic density functional theory (DFT) as implemented in the Vienna ab initio package (VASP),[16–19] using the projector augmented wave (PAW) method,[20,21] and a plane wave basis set expanded to a kinetic energy cutoff of 400 eV. Exchange and correlation effects were considered using the generalized gradient approximation (GGA) as parameterized by Perdew, Burke, and Ernzerhof for the exchange–correlation potential.[22] The first Brillouin zone was sampled by a k-point density of at least 5 pt Å^{-1} in the x- and y-directions of the reciprocal lattice, except for some of the dynamical stability calculations which were sampled at a slightly lower density due to computational constraints.

All ordered structures were optimized until forces on atoms were converged within 0.01 eV Å^{-1}, and the total electronic energy was converged within 0.01 meV per atom. Due to computational reasons, disordered structures were optimized until the total energy was converged within 0.1 eV per ionic step and supercell. This translates to a convergence of 0.003 eV per f.u., which is still an order of magnitude smaller than the energies presented in the discussion related to Figure 5. For ordered mixed species termination the cell shape was relaxed with respect to in-plane axis lengths and angle between them using the Broyden–Fletcher–Goldfarb–Shanno (BFGS) algorithm as implemented in the SciPy python library, with gradients for the three parameters calculated by finite differences. For single species termination and disordered mixed species termination configurations, hexagonal symmetry was enforced, i.e., the two in-plane lattice vectors were constrained to be of equal lengths with a fixed angle of 120° between them. For single species terminations, the lattice parameter was optimized using the BFGS algorithm, while for disordered mixed species termination the supercell shape was optimized by fitting a third-degree polynomial to electron energy versus lattice vector length data. The out-of-plane vector was kept fixed at 22.4 Å, leaving a vacuum spacing of at least 14.9 Å.

Dynamical Stability: Dynamical stability of the fully relaxed structures was investigated using phonopy and VASP with the finite displacement method.[23] Due to the well-known problem of this method for the evaluation of force constants, and thus phonon spectra, for 2D materials, the spectra were corrected by applying constraints to the calculated force constants to ensure rotational and translational invariance by enforcing rotational and translational sum rules according to the Born-Huang condition and the Huang invariances,[24] using the hiPhive python package[25] Tests for the O single species termination structures showed that a (3×3) supercell was sufficient to avoid self-interactions, which was used for most structures. A few structures showed considerable dispersion with negative frequencies of the optical branches of lowest energy at and around the gamma point also after the above-mentioned corrections of the force constants on the (3×3) supercell. These particular structures were also calculated for a (4×4) supercell, for which the corrected phonon spectra no longer displayed any imaginary frequencies. These particular calculations were performed at a slightly lower k-point density due to the considerable computational cost of these simulations, as mentioned previously in this section. For the same reason, structures that did not display this distinct behavior of the lowest optical branches at the gamma point were not rerun for the larger supercell. Instead, the force constants were examined and the largest value for the Frobenius norm of the force constants attained from the phonopy simulation outside the spherical cut-off utilized by hiPhive was particularly noted. For all phonopy runs that displayed negative frequencies on the (3×3) supercell after correction, the absolute value of this number was larger than 0.5 eV Å^{-2}, while for most other runs it was smaller. Table S3 (Supporting Information) shows this absolute value for each phonopy run, where there is a clear correlation between the occurrence of negative frequencies in the corrected spectra and larger values of the Frobenius norm. This suggests that the (3×3) supercell is large enough for convergence for most of the considered structures, while a few require a larger supercell to account for more long-ranged interactions.

Ordered Structures: Ordered mixed species termination was constructed by distributing the terminating species in the aligned and misaligned B site configurations, respectively, with all possible combinations considered at any given concentration attainable on the single unit cell, under the assumption that the concentration must be the same on each side of the 2D flake. The structure with lowest energy for each considered termination concentration is presented in Figure S9 (Supporting Information).

Disordered Structures: Disordered structures were constructed as special quasirandom structures (SQS) on a 3×4 supercell,[26] considering only the misaligned B site configuration for the terminations. Two termination species, T_1 and T_2, were mixed evenly on both sides of the 2D flake and assumed a homogeneous mixing.

For disordered configurations, the free energy given in Equation (1) depends on temperature through the mixing entropy ΔS_q, which is defined according to:

$$\Delta S_q = -nk_B(q\ln(q) + (1-q)\ln(1-q)) \tag{3}$$

where n is the number of terminations per formula unit ($n = 2$), k_B is the Boltzmann constant, and q is the concentration of T_1-terminations.

Sample Preparation and Optical measurement: $Mo_{2/3}B_{2-x}T_z$ flakes were prepared by HF etching of $(Mo_{2/3}Y_{1/3})_2AlB_2$, followed by TBAOH intercalation and delamination, the detailed process can be found in the ref. [8]. A $Mo_{4/3}B_{2-x}T_z$ film was prepared by vacuum filtration of $Mo_{4/3}B_{2-x}T_z$ suspension with nanoporous polypropylene. A Shimadzu UV-2450 Spectrophotometer was used for absorption spectroscopy, and diluted suspension with a concentration of 0.07 mg/ml was used for absorption spectrum collection.

XPS Analysis: XPS measurements were performed on filtered $Mo_{4/3}B_{2-x}T_z$ film, cold pressed MoB and Mo powders utilizing XPS (Kratos AXIS UltraDLD, Manchester, UK) using monochromatic Al-Kα (1486.6 eV) radiation. The X-ray beam irradiated the surface of the sample at an angle of 45°, with respect to the surface and provided an X-ray spot of 300×800 µm. Charge neutralization was performed using a coaxial, low energy ($\approx$0.1 eV) electron flood source to avoid shifts in the recorded binding energy. XPS spectra were recorded for the regions Mo 3d, Y 3d, B 1s, Al 2p, O 1s, C 1s (not shown here), and F 1s for $Mo_{4/3}B_{2-x}T_z$ filtered film, Mo 3d, B 1s for MoB cold pressed sample and Mo 3d for Mo cold pressed sample. The analyzer pass energy used for all the regions was 20 eV with a step size of 0.1 eV. The BE scale of all XPS spectra was referenced to the Fermi-edge (EF), which was set to a BE of zero eV in accordance with ref. [27]. Three regions were measured on each sample. The peak fitting was carried out using CasaXPS Version 2.3.16 RP 1.6 and the global elemental percentage was quantified in the same manner as in refs. [8,10,28] as well as the calculation of the chemical formula for cold pressed MoB and the $Mo_{4/3}B_{2-x}T_z$ filtered film.

Electrochemical Characterization: The electrochemical characterization of the filtered $Mo_{4/3}B_{2-x}T_z$ film was performed in a three-electrode configuration using an SP-300 potentiostat (Bio-Logic Science Instruments), controlled from a computer using the EC-Lab software. 10 µL of a colloidal suspension of $Mo_{4/3}B_{2-x}T_z$ was drop cast onto glassy carbon (GC) (5 mm diameter, SIGRADUR G from HTW Hochtemperatur-Werkstoffe GmbH) substrates to achieve a mass loading of 0.1 mg cm^{-2} of active material. The drop casted $Mo_{4/3}B_{2-x}T_z$ suspension was then dried under Ar flow. On top of the dried catalyst layer, 10 µL of Nafion was added as a binder and dried again. The modified GC electrode was then mounted in a rotating disk electrode (RDE) rotor (Pine Research Instrumentation) as a working electrode, a graphite rod (3 mm, purity >99.995% from Sigma-Aldrich) as counter electrode, and a Hg/Hg_2SO_4 as a reference electrode (B3610+ from SI Analytics).

Cyclic voltammetry (CV), and chronopotentiometry (CP), electrochemical measurements were performed at room temperatures in 0.5 M H_2SO_4 prepared from 96% H_2SO_4 (Suprapur grade, Merck) and 18.2 MΩ cm Millipore water. All the potentials were converted to the reversible hydrogen electrode (RHE) based on an experimental procedure, cycling the potential of a Pt wire between −0.71 and −0.69 V versus the reference electrode in H_2-saturated 0.5 M H_2SO_4 at a 5 mV s^{-1} scan rate. The reference electrode potential shift from RHE was noted from the intercept of current axes and represents the reduction/oxidation potential for hydrogen (the RHE zero). The obtained shift in potential was found to be −0.704 V versus RHE. Before the experiments, the electrochemical glass cell and gas bubbler were cleaned in aqua regia overnight and rinsed thoroughly with 18.2 MΩ cm Millipore water to remove traces of noble metals, such as Pt which can be present on glass from previous experiments. Typical values for the measured Ohmic resistance, R_U, ranged from 7 to 9 Ω and were determined by electrochemical impedance spectroscopy (EIS) measurements. EIS was performed by applying an AC amplitude of 10.0 mV in a frequency range from 10 kHz to 10 Hz and recorded at open circuit potential (OCV) in 0.5 M H_2SO_4. The measured R_U values were used to compensate the iR drop of the potential to 85% during the measurements and the remaining 15% were corrected for in the data analysis. The hydrogen evolution reaction was analyzed at a scan rate of 50 mV s^{-1} under Ar saturated 0.5 M H_2SO_4. Similarly, reference experiments were done using 5 mm polycrystalline Pt and GC disks and conducted after the measurements of the $Mo_{4/3}B_{2-x}T_z$ material.

Supporting Information

Supporting Information is available from the Wiley Online Library or from the author.

Acknowledgements

Conflict of Interest

The authors declare no conflict of interest.

Data Availability Statement

The data that support the findings of this study are available from the corresponding author upon reasonable request.

Keywords

[1] K. S. Novoselov, A. K. Geim, S. V. Morozov, D. Jiang, Y. Zhang, S. V. Dubonos, I. V. Grigorieva, A. A. Firsov, *Science* **2004**, *306*, 666.
[2] D. Pacilé, J. C. Meyer, Ç. Ö. Girit, A. Zettl, *Appl. Phys. Lett.* **2008**, *92*, 133107.
[3] M. Chhowalla, H. S. Shin, G. Eda, L.-J. Li, K. P. Loh, H. Zhang, *Nat. Chem.* **2013**, *5*, 263.
[4] M. Naguib, M. Kurtoglu, V. Presser, J. Lu, J. Niu, M. Heon, L. Hultman, Y. Gogotsi, M. W. Barsoum, *Adv. Mater.* **2011**, *23*, 4248.
[5] A. VahidMohammadi, J. Rosen, Y. Gogotsi, *Science* **2021**, *373*, 372.
[6] X. Guo, S. Lin, J. Gu, S. Zhang, Z. Chen, S. Huang, *Adv. Funct. Mater.* **2021**, *31*, 2008056.
[7] Z. Jiang, P. Wang, X. Jiang, J. Zhao, *Nanoscale Horiz.* **2018**, *3*, 335.
[8] J. Zhou, J. Palisaitis, J. Halim, M. Dahlqvist, Q. Tao, I. Persson, L. Hultman, P. O. Å. Persson, J. Rosen, *Science* **2021**, *373*, 801.
[9] M. Dahlqvist, J. Rosen, Q. Tao, J. Zhou, J. Palisaitis, P. O. Å. Persson, *J. Am. Chem. Soc.* **2020**, *142*, 18583.
[10] H. Lind, J. Halim, S. I. Simak, J. Rosen, *Phys. Rev. Mater.* **2017**, *1*, 44002.
[11] Q. Tao, M. Dahlqvist, J. Lu, S. Kota, R. Meshkian, J. Halim, J. Palisaitis, L. Hultman, M. W. Barsoum, P. O. Å. Persson, J. Rosen, *Nat. Commun.* **2017**, *8*, 14949.
[12] W. E. Moddeman, A. R. Burke, W. C. Bowling, D. S. Foose, *Surf. Interface Anal.* **1989**, *14*, 224.
[13] P. C. K. Vesborg, T. F. Jaramillo, *RSC Adv.* **2012**, *2*, 7933.
[14] W. Yuan, L. Cheng, Y. An, H. Wu, N. Yao, X. Fan, X. Guo, *ACS Sustainable Chem. Eng.* **2018**, *6*, 8976.
[15] H. Lind, B. Wickman, J. Halim, G. Montserrat-Sisó, A. Hellman, J. Rosen, *Adv. Sustainable Syst.* **2021**, *5*, 2000158.
[16] G. Kresse, J. Hafner, *Phys. Rev. B* **1994**, *49*, 14251.
[17] G. Kresse, J. Furthmüller, *Comput. Mater. Sci.* **1996**, *6*, 15.
[18] G. Kresse, J. Hafner, *Phys. Rev. B* **1993**, *47*, 558.
[19] G. Kresse, J. Furthmüller, *Phys. Rev. B* **1996**, *54*, 11169.
[20] P. E. Blöchl, *Phys. Rev. B* **1994**, *50*, 17953.
[21] G. Kresse, D. Joubert, *Phys. Rev. B* **1999**, *59*, 1758.
[22] J. P. Perdew, K. Burke, M. Ernzerhof, *Phys. Rev. Lett.* **1996**, *77*, 3865.
[23] A. Togo, I. Tanaka, *Scr. Mater.* **2015**, *108*, 1.
[24] M. Born, K. Huang, *Dynamical Theory of Crystal Lattices*, Oxford University Press, Oxford.
[25] F. Eriksson, E. Fransson, P. Erhart, *Adv. Theory Simul.* **2019**, *2*, 1800184.
[26] A. Zunger, S.-H. Wei, L. G. Ferreira, J. E. Bernard, *Phys. Rev. Lett.* **1990**, *65*, 353.
[27] G. Greczynski, L. Hultman, *Prog. Mater. Sci.* **2020**, *107*, 100591.
[28] J. Halim, K. M. Cook, P. Eklund, J. Rosen, M. W. Barsoum, *Appl. Surf. Sci.* **2019**, *494*, 1138.